

---

# Tritium Migration to the Surfaces of Aluminum 6061, Oxygen-Free, High-Conductivity Copper, and Stainless-Steel 316

## Introduction

Tritium is a widely used hydrogen isotope with applications ranging from nuclear fusion to use as a radioactive label in the development of drugs.<sup>1</sup> When exposed to metal surfaces, tritium will undergo isotopic exchange with any hydrogen-containing species adsorbed on the surface, such as small organic molecules and water.<sup>2</sup> Because of this effect, the surface layer of an adsorbed material can contain large concentrations of tritium.<sup>3</sup> Tritium also dissolves in metal lattices,<sup>4–6</sup> where it occupies interstitial lattice sites, vacancies, etc. Tritium concentrations within the metal lattice are much lower than the corresponding surface concentrations.

Once removed from the tritium-gas environment, a contaminated metal will continue to outgas tritium for prolonged periods of time.<sup>7</sup> During this outgassing process, tritium first desorbs from the surface; then the tritium present in the metal lattice replenishes the depleted surface activity. Surface replenishment is diffusion limited and assumed to be much slower than tritium outgassing under ambient conditions.

The absorption of hydrogen isotopes by metals is preceded by adsorption onto the metal surface. While adsorption is a key step in the overall absorption of tritium, several fundamental aspects of the process remain unknown. A better understanding of the physical processes could lead to the development of effective tritium adsorption/absorption barriers, which is of particular interest for nuclear fusion reactors and a future hydrogen economy.

The present study has measured the replenishment of surface activity on stainless-steel 316, aluminum 6061, and oxygen-free, high-conductivity (OFHC) copper by selective removal of surface-bound tritium using an argon plasma. The migration of tritium to the surface is calculated with a diffusion model developed by the authors. This model calculates the solubility of tritium on the surface of each metal and the plasma-removal efficiency.

## Experimental Setup and Procedures

Metal samples, with dimensions of  $5.1 \times 1.8 \times 0.3$  cm, were charged with tritium by exposing them to  $\sim 1$  atm of deuterium-tritium (DT) gas at  $25^\circ\text{C}$ . Table 141.IV details the exposure conditions. The loading apparatus contained multiple slots, which allowed for simultaneous loading of a set of samples while keeping each sample separate from its neighbors. Two different sets of samples were charged with tritium and then stored in a helium environment. The first set of samples contained only stainless steel; these samples were stored together in the same metallic container until each experiment. Individual samples were removed using a glove bag to retain the helium environment in the storage vessel. The second loading set contained stainless steel, copper, and aluminum samples. These samples were stored in individual containers until each experiment, which eliminated the use of a glove bag. Each sample was exposed to laboratory air briefly while loading it into the plasma chamber.

Several samples from each set were subjected to thermal desorption to determine the total activity.<sup>8</sup> Set #1 samples

Table 141.IV: Sample loading conditions. Samples were stored under helium. Set #1 samples were stored in the same container and removed using a glove bag; Set #2 samples were stored in separate containers.

Set	Time (h)	DT pressure (Torr)	T:D ratio	Storage time	Metal
1	3	686.8	45%	3.5 yrs	Stainless-steel 316
2	24	659.0	39%	$\leq 36$ days	Al, Cu, stainless-steel 316

contained ~200  $\mu\text{Ci}$ , whereas Set #2 samples contained 700 to 900  $\mu\text{Ci}$ , depending on the metal type.

Each sample was suspended inside a 2-L vacuum chamber that was purged with a flowing stream of argon at a pressure of 8 Pa (Fig. 141.57). A Tonks–Langmuir plasma<sup>9</sup> was ignited by passing a 13.56-MHz alternating current through a copper coil wrapped around the exterior of the glass vacuum chamber. Argon ions generated in the plasma were assumed to have a Maxwellian distribution with an average temperature of 298 K. These ions were accelerated toward the metal samples after crossing a sheath surrounding the sample to strike the surface with an energy of the order of 10 eV. The ion impact sputtered tritiated compounds from the surface. Tritium removed from the samples was monitored downstream of the vacuum chamber in real time by using an in-line tritium monitor (TM).<sup>10</sup>

The sample temperature was measured using an uncontaminated metal sample. The temperature increased by less than 1°C during 2-s plasma exposures. All samples were assumed to remain at room temperature throughout the decontamination sequence.

Between each plasma exposure, the sample was kept under the argon flow for various dwell periods. A layer of water

redeposited on the metal surfaces during these dwell periods within 0.5 s because the base pressure of the vacuum system was of the order of 1 Pa.

The tritium diffusion rate in the three metals is low at room temperature. The mean distance that a triton will travel through the metal lattice is

$$\langle x \rangle = \sqrt{4 * D * t}, \quad (1)$$

where  $D$  is the bulk diffusion coefficient assumed to be constant during the plasma exposure time  $t$ . Using the best-fit values for solubility and diffusivity for each metal (discussed in the **Appendix**, p. 69), the maximum amount of activity from the bulk that could be released during a plasma exposure is calculated by

$$A = \langle x \rangle * SA * S * N_{\alpha} * \lambda, \quad (2)$$

where  $SA$  is the surface area of the sample,  $S$  is the molar tritium concentration in the bulk at the end of the storage period,  $\lambda$  is the decay constant for tritium, and  $N_{\alpha}$  is Avogadro’s number. The estimates are compared against the activity  $A_{\text{data}}$  removed during the first plasma exposure of each metal in Table 141.V and show that the triton contribution from the bulk to the total

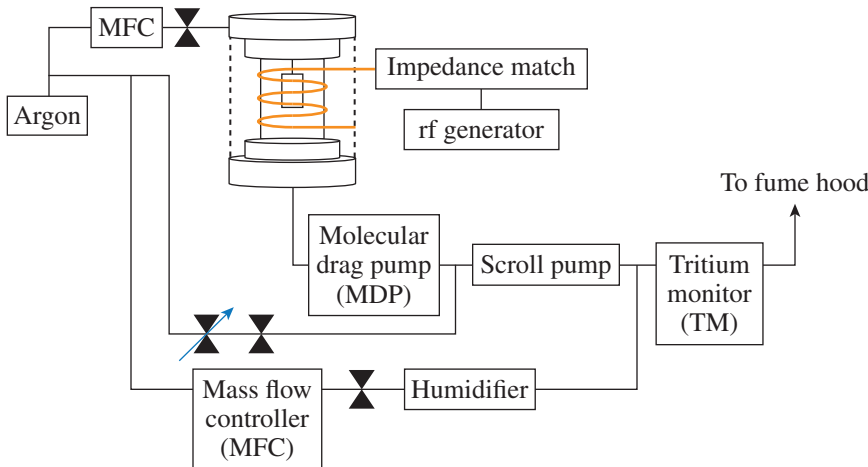


Figure 141.57  
Diagram of the plasma system. Two gas lines are necessary for operating the tritium monitor (TM). A humid purge line reduces the memory effect of tritium in the TM. An additional dry purge line reduces the residence time of gas in the TM. rf: radio frequency.

E23798JR

Table 141.V: Calculated maximum activities  $A_{\text{cal}}$  that can be removed during a single plasma exposure, assuming the surface and bulk metal concentrations are in equilibrium.

Metal	$\langle x \rangle$ ( $\mu\text{m}$ )	$A_{\text{cal}}$ ( $\mu\text{Ci}$ )	$A_{\text{data}}$ ( $\mu\text{Ci}$ )
Aluminum	7.97	3.1	21 $\pm$ 6
Copper	1.04	0.4	31 $\pm$ 6
Stainless-steel 316	0.06	0.5	52 $\pm$ 6

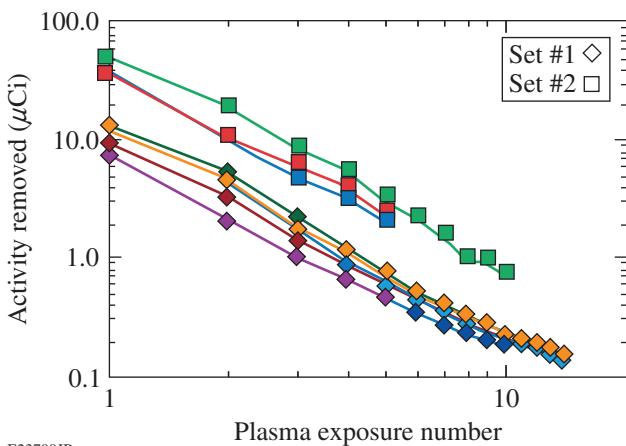
activity released in the first plasma exposure is 15%, 1%, and 1% for aluminum, copper, and stainless steel, respectively.

These 2-s exposures provided a controlled method for selective removal of surface-bound tritium without any significant contribution from the bulk. Table 141.V indicates that for all metal samples, the maximum activity released from the bulk during a 2-s plasma exposure is expected to be small compared to the activity present on the surface and is below the resolution of the experiment. Triton contributions from the bulk to the total activity released from a sample during a 2-s exposure are neglected in the analysis that follows.

**Results**

Tritium release from stainless-steel surfaces during a series of 2-s plasma exposures is shown in Fig. 141.58 on a log-log plot for both loading sets. The initial activity present on each surface determines the magnitude of the activity removed during each exposure series. Set #2 samples, which are loaded for a longer time and stored for a shorter time, have more surface activity than samples from Set #1. The trend in the quantity of activity removed with each successive plasma exposure appears similar for both sets, even though the initial activity removed from each sample differs.

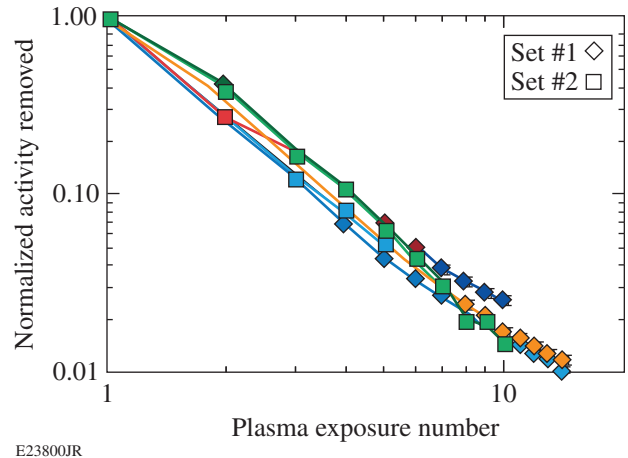
To compare the activity-removal trends for each sample, the dependence on the initial activity was removed by normalizing the data to the initial activity removed in each series of plasma exposures. This was done by dividing each data series by the initial activity removed. The normalized data are replotted in Fig. 141.59. These data indicate that the trend in activity



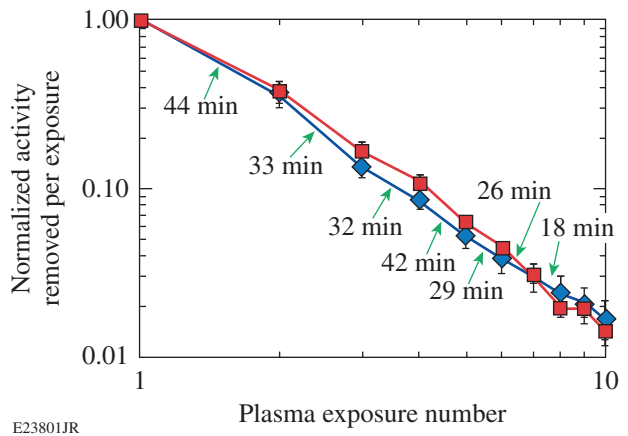
E23799JR  
Figure 141.58  
Activity removed from stainless-steel samples during a series of 2-s plasma exposures.

removed in sequential exposures does not depend on either the loading conditions or the storage time.

Figure 141.60 illustrates the dependence of the normalized amount removed on the dwell period between plasma shots. The dwell period between plasma exposures of stainless-steel samples was varied between 10 to 100 min for samples from the first loading set but was fixed at a constant 20 min for the second set of samples. This plot compares the response from two samples for clarity; it is representative of all the other data sets.



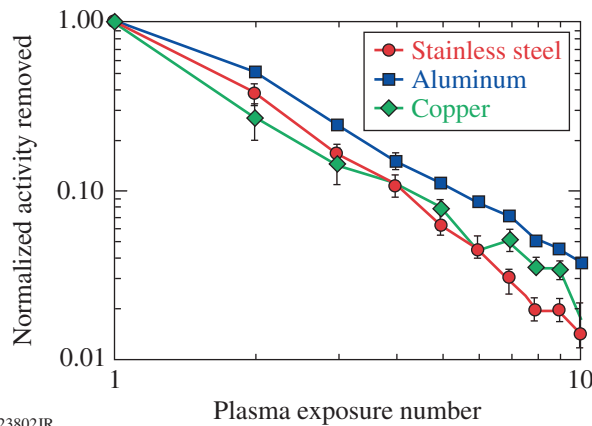
E23800JR  
Figure 141.59  
Activity removed from stainless steel in sequential exposures. The data were normalized to the initial activity removed for samples charged with DT under different conditions.



E23801JR  
Figure 141.60  
Dependence of activity removed from stainless-steel samples on variable dwell periods between plasma shots. A 20-min dwell period was used for the sample from Set #2 (red squares). The dwell period for the second sample (blue diamonds) varied between 18 and 44 min.

Decreasing the dwell period from 100 min to 10 min had no effect on the dependence of the normalized amount of activity removed with successive plasma exposures.

Normalized activities removed by sequential 2-s plasma exposures from aluminum and copper surfaces are compared to stainless steel in Fig. 141.61. Within experimental error, the same trend is observed in both aluminum and copper as in stainless steel.



E23802JR

Figure 141.61 Comparison of the dependence of normalized activity removed from aluminum, copper, and stainless-steel samples on sequential plasma exposures for samples from Set #2

**Discussion**

Tritium dissolves in metals by dissociating into atoms and then occupying interstitial locations, defect sites, and grain boundaries within the bulk metal.<sup>11,12</sup> On the surface, tritium atoms isotopically exchange with protons present in adsorbed water layers. An illustration of the tritium-metal system is shown in Fig. 141.62. The metal-oxide layer, which forms between the hydroxyl layer and metal surface, has been omitted for simplicity. The hydroxyl groups bound to the bulk metal have spacing equal to the metal lattice parameter. This spacing arises because the oxygen atoms in the hydroxyl ion bind to a location directly on top of each metal center.<sup>13</sup>

The first layer of molecular water to adsorb is rigidly proton bonded to the hydroxyl layer.<sup>14</sup> This layer is not removable by purging with a dry gas alone.<sup>15</sup> Subsequent layers of adsorbed water become more mobile as the number of layers increases. The overall number of water layers on the metal surface is determined by an isotherm<sup>16-18</sup> that correlates with the water vapor pressure present over the metal surface, the metal in question, and the ambient temperature. The isotopic composition of

Absorbed water layer		Bulk metal			
HO	M	M	T	M	
H <sub>2</sub> O		M	M		
TO	M	T	M		M
HTO		M	T	M	
TO	M		M		M
H <sub>2</sub> O		M		M	
HO	M	T	M		M
HTO		M		M	
TO	M		M		M
H <sub>2</sub> O		T	M	T	M
HO	M		M		M

E23803JR

Figure 141.62 Illustration of the surface structure present on metals, including potential tritium locations within each media but excluding the native oxide layer between the base metal and the hydroxyl layer.

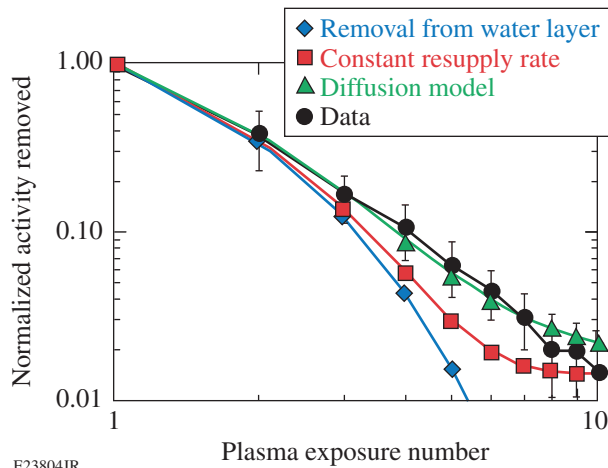
these outer layers of water is not expected to depend strongly on the substrate metal.

Short plasma exposures remove the tritium-rich water layers from the metal surface. Between plasma exposures, these water layers are quickly replaced by tritium-free water, as discussed above. During the dwell period, tritium is expected to migrate into the newly adsorbed water layers on the surface, driven by the tritium concentration gradient across the surface/bulk interface.

Three potential mechanisms may account for the tritium released during a series of plasma exposures:

1. The removable tritium inventory resides in the water/oxide layers and re-equilibrates within those layers during the dwell period.
2. Tritium migrates from the bulk into the surface layers at a constant rate.
3. The surface layers are replenished with tritium by Fickian diffusion from the bulk.

The predicted amount of activity removed in sequential plasma exposures based on each of these scenarios is compared against experimental data in Fig. 141.63.



E23804JR

Figure 141.63

The plot compares different triton-accumulation scenarios in the water layer on a Set #2 stainless-steel sample. All calculations assumed a plasma efficiency of 65%. Error bars reflect the observed spread in the data.

If the entire tritium inventory released during the plasma-exposure sequence resides in the water layer on the metal surface, the amount of activity removed during a sequence should follow the relation

$$R_i = A_0 * (1 - \varepsilon)^{i-1} * \varepsilon, \quad (3)$$

where  $A_0$  is the initial surface activity,  $i$  is the plasma-exposure number, and  $\varepsilon$  is the plasma-removal efficiency. The efficiency  $\varepsilon$  represents the fraction of tritium removed during a plasma exposure and is assumed to be constant throughout a series of exposures. This activity removal rate grossly underpredicts the experimental data shown in Fig. 141.63 and suggests that there is a replenishment of tritons from the bulk during the dwell period.

Including a constant rate of tritium migration from the bulk metal to the surface during the dwell period, the activity removed in the series of plasma exposures can be represented by

$$A_i = A_{i-1} * (1 - \varepsilon) + C, \quad (4)$$

$$r_i = A_{i-1} * \varepsilon, \quad (5)$$

where  $C$  is the amount of tritium migrating into the surface during a constant dwell period,  $A_i$  is the activity remaining after each plasma exposure, and  $r_i$  is the activity removed during exposure  $i$ .

Figure 141.63 shows that this calculation also underpredicts the activity removed during an exposure sequence, albeit to a lesser extent than that predicted by Eq. (3). In addition, after the eighth exposure, the calculated activity removed approaches a limiting value—a behavior that is not observed experimentally.

Figure 141.63 shows that the best fit to the data occurs for the third scenario, in which the surface is replenished with tritium by Fickian diffusion from the bulk. In this case, the quantity of activity removed during a plasma exposure is given by the residual surface activity and the quantity of activity that diffused into the surface layer during the dwell period:

$$A_i = [A_{i-1} * (1 - \varepsilon) - F * SA * \Delta t] * \varepsilon, \quad (6)$$

where  $A_i$  is the activity removed during exposure  $i$ ,  $F$  is the diffusion flux  $[\partial^2 c(x, t) / \partial x^2]$  at the surface/bulk interface,  $SA$  is the sample surface area,  $\Delta t$  is the dwell period between plasma exposures, and  $\varepsilon$  is the plasma-removal efficiency.

In this case the tritium migration rate to the surface was estimated by calculating the concentration profiles throughout the metal. These profiles were calculated assuming Fickian diffusion<sup>19</sup> and take several factors into account:

1. There is a metallurgical bond between the surface layers and the bulk metal.
2. The rate at which the samples incorporate tritium during loading is also limited by diffusion into the metal.
3. Tritium equilibrates within the bulk during the storage time between loading the samples and exposing the plasma.
4. Tritium-concentration profiles beneath the water layer develop in the bulk metal as the tritons are transferred from the bulk to the water layer.

Triton diffusion from the bulk to the water layer must cross the surface/bulk interface. Assuming that there is a metallurgical bond between the metal substrate and the water layer closest to the metal surface, the tritium concentrations on either side of the surface/bulk interface are related through the ratio of their respective solubility as shown in Eq. (7):

$$C_{\text{surface}} = \frac{S_{\text{surface}}}{S_{\text{bulk}}} * C_{\text{bulk}} = S * C_{\text{bulk}}. \quad (7)$$

Simulating the model to predict the quantity of tritium removed involved three phases: sample loading, sample storage, and plasma exposures. The surface concentration was estimated using the tritium partial pressure over the metal samples assuming it to be saturated and fixed for the duration of the loading phase. Plasma exposures were assumed to remove a constant amount of water from the surface. However, the activity of the surface water depended on the tritium concentration in the bulk at the surface/bulk interface. Finally, no tritium was assumed to be lost during the dwell period between plasma exposures or during sample storage.

Typical calculated tritium-concentration profiles immediately following each exposure for a sequence of plasma exposures are shown in Fig. 141.64 on a semi-log plot. These particular profiles were calculated for an aluminum sample from Loading Set #2 (Table 141.VI). Only the profiles after plasma exposures 1, 3, 5, 7, and 9 are shown for clarity. Given the high diffusivity of aluminum at room temperature, the

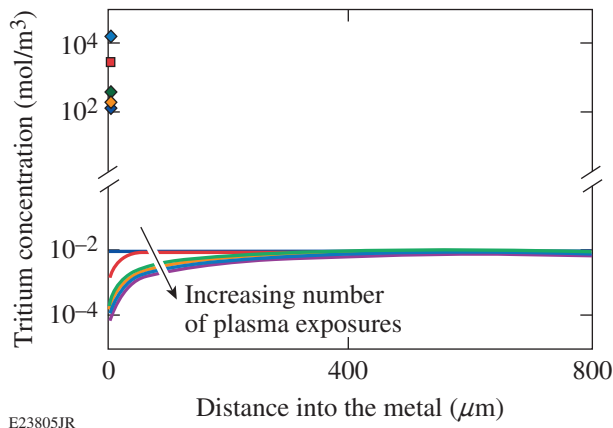


Figure 141.64  
Calculated tritium-concentration profiles in aluminum after plasma exposures 1, 3, 5, 7, and 9. The initial profile prior to the first exposure is also shown.

Table 141.VI: Lattice diffusivity and solubilities calculated from a collection of literature references. Values reported here are for 25°C.

Metal	Diffusivity (m <sup>2</sup> /s)	Solubility (mol T/m <sup>3</sup> /atm <sup>1/2</sup> )
Aluminum	$7.95 \times 10^{-12}$	0.044
Copper	$1.32 \times 10^{-13}$	0.220
Stainless-steel	$3.76 \times 10^{-16}$	2.020

initial concentration profile in the bulk metal reached steady state during the storage period prior to the first plasma exposure. During the 20-min dwell period between each plasma exposure, the concentration gradient in the bulk relaxed over time as tritons migrated to the surface.

In the model, the sample recovers from each plasma exposure by repopulating the tritium-deficient water layer with tritons from the bulk near the interface, as illustrated in Fig. 141.65, in an effort to re-establish the surface concentration specified by Eq. (8). However, since the tritium migration rate is diffusion limited, the tritium concentration in the water layer cannot return to its original value within the dwell period. By the ninth exposure, the surface tritium concentration has dropped from its original value of 15.2 kmol T/m<sup>3</sup> to 0.6 kmol T/m<sup>3</sup>. The corresponding bulk concentration at the

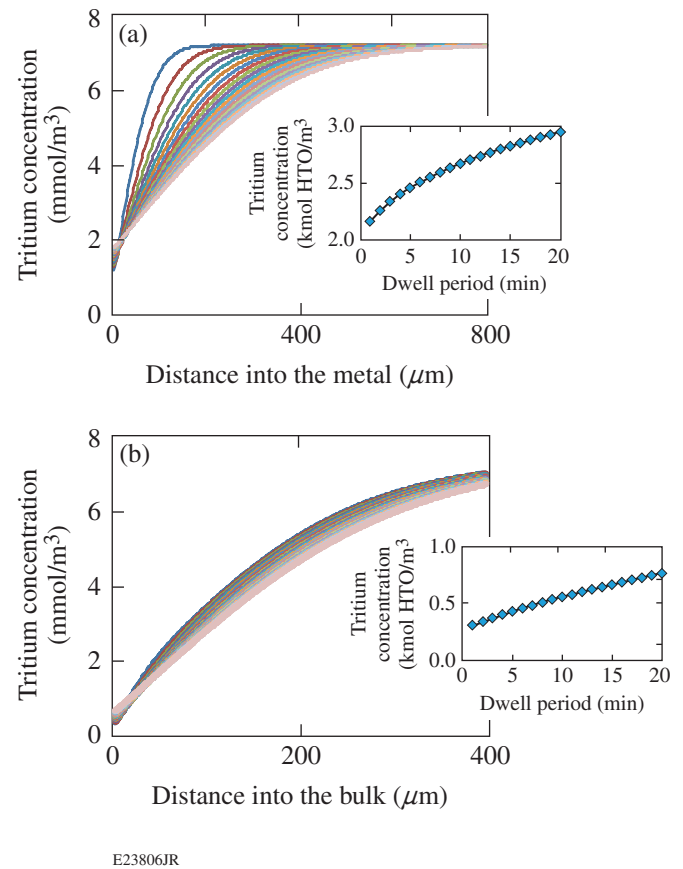


Figure 141.65  
Evolution of tritium-concentration profiles during the dwell period after plasma exposures (a) #1 and (b) #3. The insets show the increase in surface concentration during each dwell period.

interface has dropped from 7.2 mmol T/m<sup>3</sup> to 0.3 mmol T/m<sup>3</sup>, at which point the perturbed concentration depth profile extends ~75% to the center of the sample.

The diffusivity and solubility for each metal at 25°C are provided in Table 141.VI. These values represent the “best fit” computed from a compilation of literature references that are discussed in the **Appendix** (p. 69).

As an aside, extrapolating the lattice solubility of copper from high-temperature data ( $\geq 200^\circ\text{C}$ ) to room temperature underpredicts the effective hydrogen solubility in copper. The effective solubility is dominated by the significant number of shallow traps, defects, and vacancies present in copper.<sup>20–22</sup> Since the hydrogen binding energies in copper at defect sites and octahedral sites are similar,<sup>23</sup> the effective hydrogen diffusivity through copper at temperatures below 200°C does not deviate from the Arrhenius behavior extrapolated from higher temperatures.<sup>24</sup>

The model was fit to the data by varying both the plasma-removal efficiency and the surface-to-bulk solubility ratio. The results of the fits for the three metals are shown in Table 141.VII. Published isotherms were used to determine the water-layer thickness, but the values reported here include an additional proton-bonded monolayer, as discussed above. A graphical comparison between the model predictions and data is provided in Fig. 141.63.

Table 141.VII: Solubilities for tritium in the water layer on metal surfaces as derived from model fits to experimental data. Surface thicknesses of the water layers were calculated from the water isotherms published for these metals.

Metal	Surface thickness (nm)	Surface-layer solubility (kmol T/m <sup>3</sup> )	Plasma-removal efficiency
Aluminum	0.54	53±2.0	0.85±0.05
Copper	0.54	50±1.0	0.56±0.05
Stainless-steel	0.92	17.5±0.3	0.66±0.05

The surface solubilities for each metal reported in Table 141.VII were calculated from the bulk metal solubility and the solubility ratio provided by Eq. (8). The surface solubilities for all three metals are similar, as expected. Additionally, they are less than the absolute maximum, which is estimated to be  $\approx 100$  kmol/m<sup>3</sup>. The absolute maximum is calculated by counting the total number of protons on the surface for a given relative humidity:

$$S_{\text{surface}} = S * S_{\text{bulk}} \quad (8)$$

Figure 141.66 shows the effect of varying the plasma-removal efficiency from 0.60 to 0.70 while holding the solubility ratio constant in the diffusion model. In this figure, the model is compared against a representative data set for a stainless-steel sample from Loading Set #2. The error bars reflect the observed spread in the data reported in Fig. 141.59 and do not include systematic errors in the data. This analysis suggests the removal efficiency is known to within  $\pm 5\%$ . Tritium is removed from aluminum surfaces with the highest efficiency, while removal from copper surfaces is the lowest.

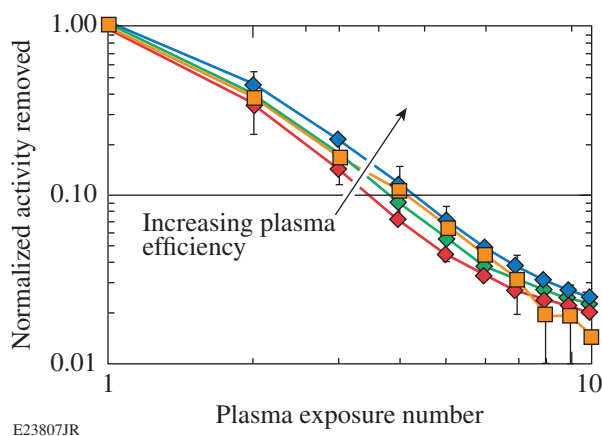


Figure 141.66

Comparison of the normalized activity removed from a Set #2 stainless-steel sample with the model for various plasma efficiencies. Data are shown as square points.

## Conclusions

The experimental data show that low-pressure argon plasma is an effective tool in studying how tritium migrates from the bulk to the surface as tritium is removed from metal surfaces. Tritium is removed in decreasing quantities with successive plasma exposures, which suggests a depletion of the surface and near-surface tritium inventories. This trend in activity removed does not depend on dwell periods of less than 100 min, loading and storage conditions, or substrate metal.

The output of the diffusion model presented here confirms previous findings that the water layers on a metal surface provide a huge storage capacity for tritium. The concentration ratio across the water layer/bulk metal interface is uniquely determined by the solubility ratio across this interface. Perturbing the surface concentrations of tritons by replacing a tritium-rich water layer with a tritium-free water layer induces the tritium-

deficient water layer to “pump” tritium from the bulk to the surface in an effort to re-establish its previous equilibrium state. This process is driven by a concentration gradient that develops in the bulk because of the perturbation.

The model effectively describes tritium transport into and out of stainless steel, aluminum, and oxygen-free, high-conductivity copper when these metals are exposed to a tritium partial pressure at room temperature:

1. The surface water layer rapidly saturates with tritium to values that are determined by the exposure conditions.
2. The bulk metal accepts tritium from the saturated tritium-rich water layer on the surface at a rate determined by the diffusivity of the base metal.
3. The surface tritium concentration equilibrates with the bulk concentration to a unique value determined by the metal solubility for hydrogen.
4. Tritium transport from the bulk can be encouraged via lattice diffusion or shallow traps by replacing the tritium-rich water layers on the surface with tritium-deficient water layers. This transport rate is determined by the diffusivity of the base metal.

Comparing the model predictions with data suggests that the tritium-concentration equilibration time constant within the water layers on the surface of these metals is significantly shorter than expected from the diffusivity in the bulk metal.

## Appendix

The diffusivity and solubility have been measured for hydrogen isotopes in aluminum, copper, and stainless steel by a large number of investigators. Their data have been compiled in Tables 141.VIII–141.XIII below for each of the three metals of interest. The tables provide the pre-exponent, activation energy, and the temperature range over which the investigation was carried out. Additionally data have been plotted in Figs. 141.67–141.72 for each metal using the values in the tables in the following equation:

$$x(T) = x_0 * \exp\left(-\frac{E_\alpha}{R * T}\right),$$

where  $E_\alpha$  is the activation energy in kJ/mol,  $x_0$  is the frequency factor in  $\text{m}^2/\text{s}$  for diffusivity, and  $\text{mol}/\text{m}^3 * \sqrt{\text{atm}}$  for solubility.

The “best-fit” values for diffusivity were determined by fitting the Arrhenius equation to the collection of data by varying the activation energy and frequency factor. The best-fit (average) values are presented in Tables 141.VIII–141.X. Best-fit curves using these values are plotted in Figs. 141.67–141.69.

The best-fit values for solubility were determined by computing the mean activation energy and frequency factors for each metal and are shown in Tables 141.XI–141.XIII. Best-fit curves using these values are plotted in Figs. 141.70–141.72. This approach yielded a better representation for the best-fit solubility curves for each metal than using a fitting routine as was done for determining the best-fit diffusivity values.

Several of the references in this collection were not included when the best fits were calculated because the data did not follow the same trend established by the remaining collection. The omitted references are highlighted in the tables and relevant figures. Three references were excluded from the collection of diffusivity values in aluminum. Two of these datasets were several orders of magnitude smaller than the rest of the collection. The third data set used an activation energy that differed considerably from other investigators. The higher activation energy suggests that trapping may have played an important role in the samples used by these investigators when measuring the hydrogen diffusivities in stainless steel.

The collection of solubility measurements for the three metals showed considerably more spread than the diffusivity measurements and points to the sensitivity between hydrogen solubility and the actual character of the bulk metal. While this spread is significant, the reported values for stainless steel and copper follow a similar trend. Although the frequency factor varies from study to study, the reported activation energies are similar. All references collected for stainless steel and copper were used to determine the best-fit values. Published measurements for hydrogen solubility in aluminum are considerably more sparse. Additionally, these studies use very different activation energies for hydrogen diffusion in aluminum. These best-fit values were computed with preference given to the most-recent studies.

Reiter *et al.*,<sup>25</sup> and more recently Causey *et al.*,<sup>20</sup> reviewed the tritium interactions with metals for fusion applications. There is good agreement between the Causey’s best-fit datasets and the one presented here with exception to hydrogen diffusivities in copper and aluminum and the hydrogen solubility in aluminum. The differences are attributed to the size of the datasets used.

The hydrogen solubility values reported in Tables 141.XI–141.XIII below are calculated from measurements at elevated temperatures where hydrogen dissolution in the crystal lattice dominates. Contributions from vacancies, traps, and grain boundaries tend to be minor. Extrapolation from these temperatures, typically above 150°C, to room temperature can underpredict the actual hydrogen solubility, particularly in metals with low lattice solubilities like copper where the binding energies at the trap sites are similar to the binding energy

within the lattice.<sup>20,22,23</sup> The effective hydrogen solubility in copper has been estimated to be of the order of 1000× the lattice solubility extrapolated from high temperatures to room temperature for the calculations used in this article.

Two observations suggest that the extrapolation of the hydrogen solubility at copper lattice sites from higher temperatures to room temperature underpredicts the actual solubility at room temperature. First, using a value based solely on lat-

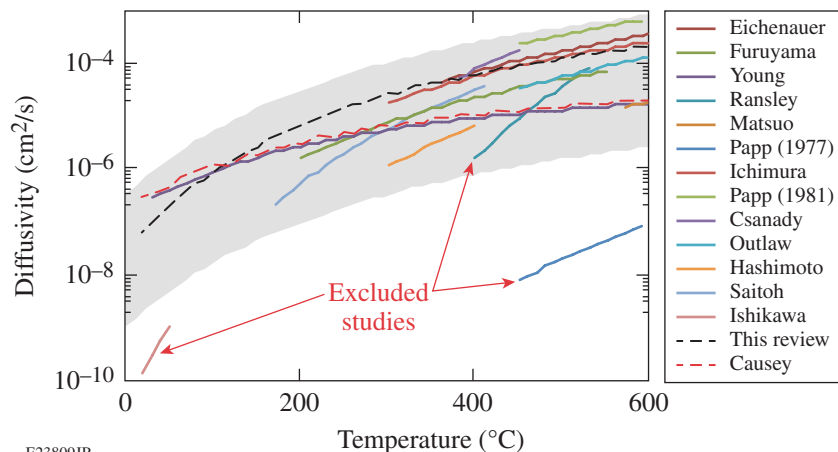


Figure 141.67  
Collection of diffusivities for hydrogen isotopes in aluminum.

E23809JR

Table 141.VIII: Literature collection of diffusivities for aluminum.

Frequency factor (m <sup>2</sup> /s)	Activation energy (kJ/mol)	Temperature range (°C)	Author (year)
$1.1 \times 10^{-5}$	40.9	360 to 630	Eichenauer (1961) <sup>26</sup>
$1.4 \times 10^{-6}$	35.7	200 to 560	Furuyama (1986) <sup>27</sup>
$1.75 \times 10^{-8}$	16.2	30 to 600	Young (1998) <sup>12</sup>
<b>12</b>	<b>140.0</b>	<b>400 to 530</b>	<b>Ransley (1955)<sup>28</sup></b>
$2 \times 10^{-6}$	50.2	570 to 630	Matsuo (1967) <sup>29</sup>
<b><math>2.5 \times 10^{-6}</math></b>	<b>90.0</b>	<b>450 to 590</b>	<b>Papp (1977)<sup>30</sup></b>
$4.58 \times 10^{-6}$	37.0	300 to 640	Ichimura (1979) <sup>31</sup>
$1.9 \times 10^{-5}$	40.0	450 to 590	Papp (1981) <sup>32</sup>
$1.30 \times 10^{-3}$	67.0	375 to 450	Csanady (1981) <sup>33</sup>
$1.01 \times 10^{-5}$	47.7	450 to 625	Outlaw (1982) <sup>6</sup>
$2.6 \times 10^{-5}$	58.7	300 to 400	Hashimoto (1983) <sup>34</sup>
$6.1 \times 10^{-5}$	54.8	173 to 408	Saitoh (1994) <sup>35</sup>
<b><math>9.2 \times 10^{-5}</math></b>	<b>55.25</b>	<b>12 to 55</b>	<b>Ishikawa (1986)<sup>36</sup></b>
$2 \times 10^{-8}$	16.0	—	Causey (2009) <sup>20</sup>
$1.45 \times 10^{-6}$	30.0	—	Average

tice solubility suggests the total initial surface activity will be  $0.39 \mu\text{Ci}$  for the exposure conditions discussed here. However, the actual activity removed during the first plasma exposure of a copper sample was tenfold higher,  $31.4 \pm 0.6 \mu\text{Ci}$ . Secondly the total tritium inventory within the copper estimated from lattice solubility underpredicts the amount released when the metal is heated to high temperatures. The total activity in the bulk was calculated by integrating the concentration profile

resulting from the semi-infinite solution to the diffusion equation. This solution used a fixed, saturated concentration at the surface/bulk interface, the mean diffusivity, and the mean lattice solubility. Summing the calculated bulk and surface activities yielded  $109 \mu\text{Ci}$ , which is  $8\times$  lower than the measured total activity of  $810 \mu\text{Ci}$ . Hydrogen storage in defect sites in the copper bulk dominates the amount stored within the lattice.

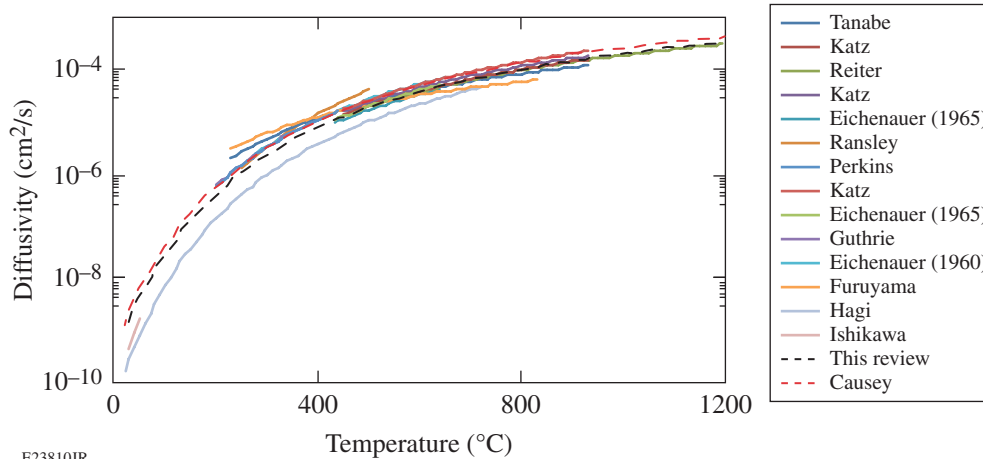


Figure 141.68  
Collection of diffusivities for hydrogen isotopes in copper.

E23810JR

Table 141.IX: Literature collection of diffusivities for copper.

Frequency factor ( $\text{m}^2/\text{s}$ )	Activation energy ( $\text{kJ/mol}$ )	Temperature range ( $^{\circ}\text{C}$ )	Author (year)
$2.26 \times 10^{-7}$	29.3	227 to 927	Tanabe (1984) <sup>4</sup>
$6.12 \times 10^{-7}$	36.5	450 to 925	Katz (1971) <sup>37</sup>
$6.6 \times 10^{-7}$	37.4	470 to 1200	Reiter (1993) <sup>25</sup>
$7.3 \times 10^{-7}$	36.8	450 to 925	Katz (1971) <sup>37</sup>
$6.2 \times 10^{-7}$	37.8	430 to 640	Eichenauer (1965) <sup>38</sup>
$6.8 \times 10^{-6}$	47.3	250 to 500	Ransley (1955) <sup>28</sup>
$1.06 \times 10^{-6}$	38.5	200 to 440	Perkins (1973) <sup>39</sup>
$1.13 \times 10^{-6}$	38.9	450 to 925	Katz (1971) <sup>37</sup>
$1.15 \times 10^{-6}$	40.8	430 to 640	Eichenauer (1965) <sup>38</sup>
$1.06 \times 10^{-6}$	38.4	200 to 440	Guthrie (1974) <sup>5</sup>
$1.1 \times 10^{-6}$	38.5	270 to 650	Eichenauer (1960) <sup>40</sup>
$8.2 \times 10^{-8}$	23.3	230 to 830	Furuyama (1986) <sup>27</sup>
$9.0 \times 10^{-7}$	43.5	-13 to 727	Hagi (1986) <sup>41</sup>
$2.74 \times 10^{-4}$	56.8	26 to 49.5	Ishikawa (1985) <sup>24</sup>
$1 \times 10^{-6}$	38.5	—	Causy (2009) <sup>20</sup>
$7.9 \times 10^{-7}$	38.6	—	Average

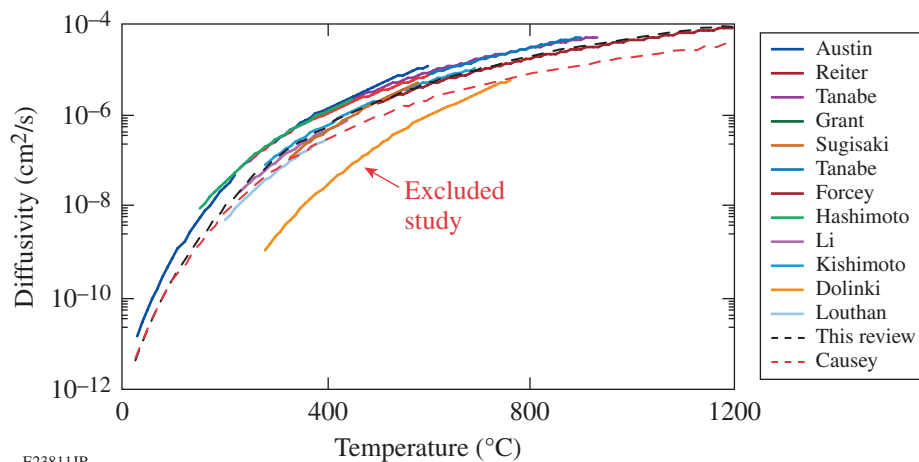


Figure 141.69  
Collection of diffusivities for hydrogen isotopes in stainless steel.

E23811JR

Table 141.X: Literature collection of diffusivities for stainless-steel 316.

Frequency factor (m <sup>2</sup> /s)	Activation energy (kJ/mol)	Temperature range (°C)	Author (year)
$1.8 \times 10^{-6}$	52.7	25 to 222	Austin (1972) <sup>42</sup>
$5.9 \times 10^{-7}$	51.9	500 to 1200	Reiter (1993) <sup>25</sup>
$6.32 \times 10^{-7}$	47.8	227 to 927	Tanabe (1984) <sup>4</sup>
$7.3 \times 10^{-7}$	52.4	276 to 692	Grant (1988) <sup>43</sup>
$4.2 \times 10^{-6}$	64.0	330 to 580	Sugisaki (1985) <sup>44</sup>
$1.74 \times 10^{-6}$	52.8	300 to 600	Tanabe (1979) <sup>45</sup>
$3.82 \times 10^{-7}$	45.5	250 to 600	Forcey (1988) <sup>46</sup>
$4.7 \times 10^{-7}$	46.3	150 to 450	Hashimoto (1985) <sup>47</sup>
$4.79 \times 10^{-7}$	51.59	230 to 440	Li (1989) <sup>48</sup>
$1.3 \times 10^{-6}$	54.0	600 to 900	Kishimoto (1985) <sup>49</sup>
$1.2 \times 10^{-5}$	85.0	227 to 757	Dolinski (2000) <sup>50</sup>
$4.7 \times 10^{-7}$	54.0	200 to 400	Louthan (1975) <sup>51</sup>
$2 \times 10^{-7}$	49.3	—	Causy (2009) <sup>20</sup>
$7.2 \times 10^{-7}$	52.9	—	Average

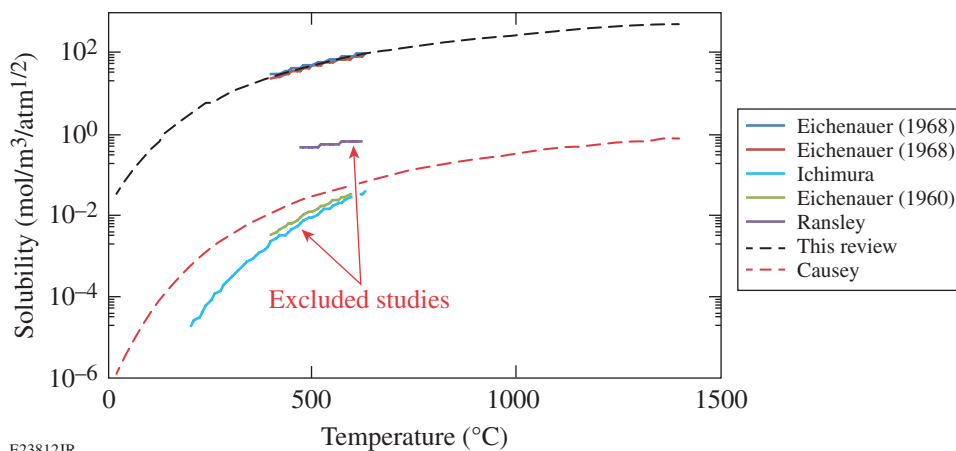


Figure 141.70  
Collection of solubilities for hydrogen isotopes in aluminum.

E23812JR

Table 141.XI: Literature collection of solubilities for aluminum.

Frequency factor (mol/m <sup>3</sup> /atm <sup>1/2</sup> )	Activation energy (kJ/mol)	Temperature range (°C)	Author (year)
3954	27.4	400 to 630	Eichenauer (1968) <sup>52</sup>
4878	29.7	400 to 630	Eichenauer (1968) <sup>52</sup>
400	63.9	200 to 630	Ichimura (1979) <sup>31</sup>
111	58.2	400 to 600	Eichenauer (1960) <sup>40</sup>
7	17.3	465 to 620	Ransley (1948) <sup>53</sup>
15	39.7	—	Causey (2009) <sup>20</sup>
4416	28.5	—	Average

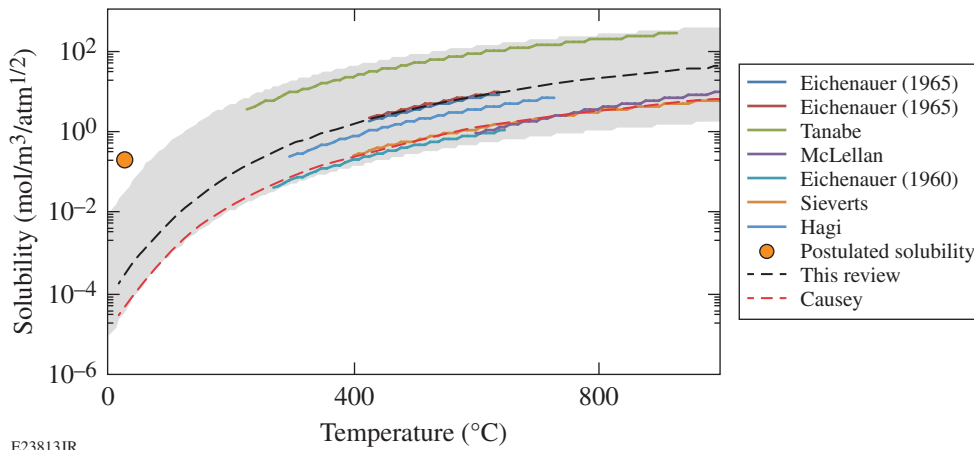


Figure 141.71  
Collection of solubilities for hydrogen isotopes in copper.

E23813JR

Table 141.XII: Literature collection of solubilities for copper.

Frequency factor (mol/m <sup>3</sup> /atm <sup>1/2</sup> )	Activation energy (kJ/mol)	Temperature range (°C)	Author (year)
1674	40.0	430 to 635	Eichenauer (1965) <sup>38</sup>
1435	38.0	430 to 635	Eichenauer (1965) <sup>38</sup>
6116	31.2	227 to 927	Tanabe (1984) <sup>4</sup>
1657	54.7	600 to 1027	McLellan (1973) <sup>54</sup>
118	36.0	270 to 650	Eichenauer (1960) <sup>40</sup>
211	37.7	400 to 1000	Sieverts (1929) <sup>55</sup>
627	37.6	287 to 727	Hagi (1986) <sup>41</sup>
252	38.9	—	Causey (2009) <sup>20</sup>
1691	39.3	—	Average

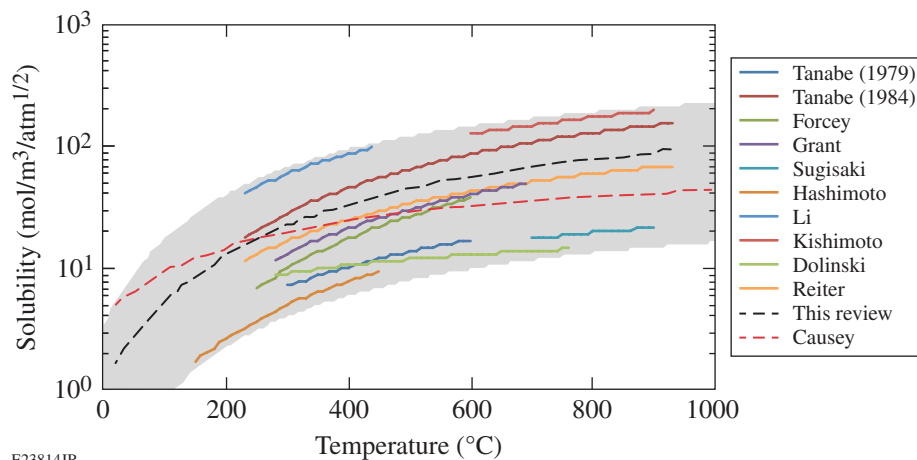


Figure 141.72  
Collection of solubilities for hydrogen isotopes in stainless steel.

E23814JR

Table 141.XIII: Literature collection of solubilities for stainless steel.

Frequency factor (mol/m <sup>3</sup> /atm <sup>1/2</sup> )	Activation energy (kJ/mol)	Temperature range (°C)	Author (year)
89	12.1	300 to 600	Tanabe (1979) <sup>45</sup>
763	15.7	227 to 927	Tanabe (1984) <sup>4</sup>
477	18.5	250 to 600	Forcey (1988) <sup>46</sup>
353	15.7	276 to 692	Grant (1988) <sup>43</sup>
62	10.2	703 to 903	Sugisaki (1984) <sup>56</sup>
103	14.5	150 to 450	Hashimoto (1985) <sup>47</sup>
820	12.5	230 to 440	Li (1989) <sup>48</sup>
719	12.5	600 to 900	Kishimoto (1985) <sup>49</sup>
26	5	277 to 757	Dolinski (2000) <sup>50</sup>
262	13.1	227 to 927	Reiter (1993) <sup>25</sup>
85	6.9	—	Causey (2009) <sup>20</sup>
342	13.0	—	Average

## REFERENCES

- C. R. Shmayda, W. T. Shmayda, and N. P. Kherani, *Fusion Sci. Technol.* **41**, 500 (2002).
- N. Nakashio *et al.*, *Fusion Sci. Technol.* **39**, 189 (2001).
- R.-D. Penzhorn *et al.*, *J. Nucl. Mater.* **353**, 66 (2006).
- T. Tanabe *et al.*, *J. Nucl. Mater.* **123**, 1568 (1984).
- J. W. Guthrie *et al.*, *J. Nucl. Mater.* **53**, 313 (1974).
- R. A. Outlaw, D. T. Peterson, and F. A. Schmidt, *Scr. Metall.* **16**, 287 (1982).
- A. B. Antoniazzi, W. T. Shmayda, and T. Palma, in *Proceedings of the 15th IEEE/NPSS Symposium on Fusion Engineering, 1993* (IEEE, New York, 1993), Vol. 2, pp. 975–978; A. B. Antoniazzi, W. T. Shmayda, and T. Palma, in *Proceedings of the 15th IEEE/NPSS Symposium on Fusion Engineering, 1993* (IEEE, New York, 1993), Vol. 2, pp. 979–982.
- M. J. Quinlan, W. T. Shmayda, S. Lim, S. Salnikov, Z. Chambers, E. Pollock, and W. U. Schröder, *Fusion Sci. Technol.* **54**, 519 (2008).
- L. Tonks and I. Langmuir, *Phys. Rev.* **34**, 876 (1929).
- N. P. Kherani and W. T. Shmayda, *Fusion Sci. Technol.* **21**, 340 (1992).
- J. K. Nørskov *et al.*, *Phys. Rev. Lett.* **49**, 1420 (1982).
- G. A. Young, Jr. and J. R. Scully, *Acta Mater.* **46**, 6337 (1998).
- J. Carrasco, A. Hodgson, and A. Michaelides, *Nat. Mater.* **11**, 667 (2012).
- P. A. Thiel and T. E. Madey, *Surf. Sci. Rep.* **7**, 211 (1987).
- M. Nishikawa *et al.*, *J. Nucl. Mater.* **277**, 99 (2000).

16. T. Ohmi *et al.*, Rev. Sci. Instrum. **64**, 2683 (1993).
17. S. P. Sharma, J. Vac. Sci. Technol. **16**, 1557 (1979).
18. H. A. Al-Abadleh and V. H. Grassian, Langmuir **19**, 341 (2003).
19. J. Crank, *The Mathematics of Diffusion* (Oxford University Press, Oxford, 1979), p. 189.
20. R. A. Causey, R. A. Karnesky, and C. San Marchi, in *Comprehensive Nuclear Materials*, 1st ed., edited by R. J. M. Konings *et al.* (Elsevier, Amsterdam, 2012), Vol. 4, pp. 511–549.
21. Å. Martinsson and R. Sandström, J. Mater. Sci. **47**, 6768 (2012).
22. M. G. Ganchenkova *et al.*, Philos. Mag. **94**, 3522 (2014).
23. P. A. Korzhavyi and R. Sandström, Comput. Mater. Sci. **84**, 122 (2014).
24. T. Ishikawa and R. B. McLellan, J. Phys. Chem. Solids **46**, 445 (1985).
25. F. Reiter, K. S. Forcey, and G. Gervasini, *A Compilation of Tritium-Material Interaction Parameters in Fusion Reactor Materials* (Commission of the European Communities, Brussels, 1993).
26. W. Eichenauer, K. Hattenbach, and A. Pebler, Z. Metallkde. **52**, 682 (1961).
27. Y. Furuyama, T. Tanabe, and S. Imoto, J. Jpn. Inst. Met. **50**, 688 (1986).
28. C. E. Ransley and D. E. J. Talbot, Z. Metallkde. **46**, 328 (1955).
29. S. Matsuo and T. Hirata, J. Jpn. Inst. Met. **31**, 590 (1967).
30. K. Papp and E. Kovács-Csetényi, Scr. Metall. **11**, 921 (1977).
31. M. Ichimura, M. Imabayashi, and M. Hayakawa, J. Jpn. Inst. Met. **43**, 876 (1979).
32. K. Papp and E. Kovács-Csetényi, Scr. Metall. **15**, 161 (1981).
33. Á. Csanády, K. Papp, and E. Pásztor, Mater. Sci. Eng. **48**, 35 (1981).
34. E. Hashimoto and T. Kino, J. Phys. F: Met. Phys. **13**, 1157 (1983).
35. H. Saitoh, Y. Iijima, and H. Tanaka, Acta Metall. Mater. **42**, 2493 (1994).
36. T. Ishikawa and R. B. McLellan, Acta Metall. **34**, 1091 (1986).
37. L. Katz, M. Guinan, and R. J. Borg, Phys. Rev. B **4**, 330 (1971).
38. W. Eichenauer, W. Löser, and H. Witte, Z. Metallkde. **56**, 287 (1965).
39. W. G. Perkins, J. Vac. Sci. Technol. **10**, 543 (1973).
40. W. Eichenauer, Memoires Scientifiques Rev. Metallurg. **LVII**, 943 (1960).
41. H. Hagi, Trans. Jpn. Inst. Met. **27**, 233 (1986).
42. J. H. Austin and T. S. Elleman, J. Nucl. Mater. **43**, 119 (1972).
43. D. M. Grant, D. L. Cummings, and D. A. Blackburn, J. Nucl. Mater. **152**, 139 (1988).
44. M. Sugisaki *et al.*, J. Nucl. Mater. **133–134**, 280 (1985).
45. T. Tanabe and S. Imoto, Trans. Jpn. Inst. Met. **21**, 109 (1980).
46. K. S. Forcey *et al.*, J. Nucl. Mater. **160**, 117 (1988).
47. E. Hashimoto and T. Kino, J. Nucl. Mater. **133–134**, 289 (1985).
48. Y. Y. Li and Z. S. Xing, J. Nucl. Mater. **169**, 151 (1989).
49. N. Kishimoto *et al.*, J. Nucl. Mater. **127**, 1 (1985).
50. Yu. Dolinski *et al.*, J. Nucl. Mater. **283–287**, 854 (2000).
51. M. R. Louthan, Jr. and R. G. Derrick, Corros. Sci. **15**, 565 (1975).
52. W. Eichenauer, Z. Metallkde. **59**, 613 (1968).
53. C. E. Ransley and H. Neufeld, J. Inst. Met. **LXXIV**, 599 (1948).
54. R. B. McLellan, J. Phys. Chem. Solids **34**, 1137 (1973).
55. A. Sieverts, Z. Metallkde. **21**, 37 (1929).
56. M. Sugisaki *et al.*, J. Nucl. Mater. **120**, 36 (1984).

